

The DeRisk database: Extreme Design Waves for Offshore Wind Turbines

Fabio Pierella^{a,*}, Ole Lindberg^b, Henrik Bredmose^a, Harry Bingham^b,
Robert W. Read^b, Allan P. Engsig-Karup^c

^a*Department of Wind Energy, DTU*

^b*Department of Mechanical Engineering, DTU*


^c*Department of Applied Mathematics and Computer Science, DTU*

Abstract

The estimation of extreme loads from waves is an essential part of the design of an offshore wind turbine. Standard design codes suggest to either use simplified methodologies based on regular waves, or to perform fully nonlinear computations. The former might not provide an accurate representation of the real extreme waves, while the latter is computationally too intensive for fast design iterations. Here, we address these limitations by using the fully nonlinear solver OceanWave3D to establish the DeRisk database, a large collected dataset of extreme waves kinematics in a two-dimensional domain. From the database, which is open and freely available, a designer can easily extract fully-nonlinear wave kinematics for a wave condition and water depth of interest by identifying a suitable computation in the database and, if needed, by Froude-scaling the kinematics.

The fully nonlinear solver is first validated against the DeRisk model experiments at two different water depths, 33.0[m] and 20.0[m], and an excellent agreement is found for the analyzed cases. The experiments are used to calibrate OceanWave3D's numerical breaking filter constant, and the best agreement is found for $\beta = 0.5$. We then compare the experimental static force with predictions obtained by the DeRisk kinematics database and the Rainey force model, and with state-of-the-art industrial practices. For milder storms, we find a good agreement in the predicted extreme force between the present methodology and all of the standard methodologies. At the deep

*Corresponding author fabpi@dtu.dk

This work is under the CC-BY-NC-ND 4.0 license 

location and for stronger storms, the largest loads are given by slamming loads due to breaking waves. In this condition, the database methodology is less accurate than the embedded stream function method and more accurate than the WiFi JIP methodology, although providing generally nonconservative estimates. For strong storms at the shallower location, where wave breaking is less dominating, the database methodology is the most accurate overall.

Keywords: wave, database, wave kinematics, nonlinear waves, monopile, force model, breaking wave, potential flow, offshore wind turbines, foundation, DeRisk

1. Introduction

The substructures for offshore wind turbines are a central element for targeted cost reductions in offshore wind energy. As rotor dimensions increase, the substructures become larger, and extreme loads from storm waves can become design drivers. Therefore, the industry needs accurate and reliable (de-risked) design methodologies for extreme waves. At present, these modelling methods fall into two camps. Either they are fast but have limited accuracy, or they are accurate but too computationally demanding for everyday design use. The main idea of this paper is to bridge this divide by establishing an extensive and openly accessible database of two-dimensional (2D) nonlinear wave kinematics, that can be used to estimate Ultimate Load States (ULS) on offshore wind turbines via integrated load modelling tools.

The IEC standards [1] presently define two different methodologies to compute nonlinear waves for extreme load evaluation. In the constrained wave approach a regular stream function wave is embedded into a background irregular linear wave realization, to account for the nonlinearity of the largest wave. For example, Rainey and Camp [2] proposed to condition the background linear sea state via the New Wave theory by Tromans et al. [3] to generate a large, linear wave at a predetermined time and location, that can be suitably replaced by a nonlinear wave. Pierella et al. [4] use the Hilbert transform to identify the embedment location and the parameters of the embedded stream function wave.

While these methodologies are intuitive and fast, they have some shortcomings. First, the largest static load is not always associated with the largest free surface elevation peak. Smaller waves can break, generating higher loads

than larger, nonbreaking waves. When the structure is inertia dominated, the force is in the first approximation proportional to the wave steepness, and the large wave is not necessarily the steepest. Secondly, real-life extreme waves usually propagate with no constant form, have nonsymmetric crests, and tend to break, violating the assumptions of stream-function theory, which only apply to symmetric regular waves on a flat bed. Moreover, to specify the height of the embedded wave, a Rayleigh distribution is assumed, and the significant wave height H_S is multiplied by a factor, e.g. 1.86 for a 3-hour (hr) realization. However the crest statistics for large nonlinear sea states do not necessarily follow a Rayleigh distribution. Lastly, especially for flexible structures, the maximum load is not necessarily associated with the largest waves [5] as it is a random combination of static and dynamic loads.

In the second suggested approach, fully nonlinear computations for a given sea state are used to assess the loads. Here, all waves are nonlinear and assumptions regarding the relationship between the free-surface elevation and the maximum induced loads are not required. Following this approach, Paulsen et al. [6] compute the loads on a stiff cylinder due to an irregular sea state on a slope via two different nonlinear methods. In the first, wave kinematics are produced via the fully nonlinear potential flow solver Ocean-Wave3D (OW3D) [7], and the loads on the structure are computed via a slender body force model. In the second, the Navier-Stokes solver OpenFoam [8] is run in a domain where the cylinder surface is directly modelled. While the two methods were able to accurately reproduce the experimental horizontal force, they respectively require 20 minutes on a single-core machine and several weeks on a computational cluster to generate a 100-second time series. It is impractical to use fully-nonlinear methods of this type to examine the many load cases considered during the design of the substructure.

In the current method, developed in the framework of the DeRisk Innovation project [9], we can retain the full nonlinearity and minimize the time needed to obtain a certain wave realization by precomputing an extensive database of extreme wave kinematics, eliminating the need for an individual to perform fully nonlinear simulations. The database is freely available in an online repository [10]. Dedicated software is provided to access the time series corresponding to the relevant site conditions, and to perform Froude-scaling where necessary. With this paper we describe the calculation and compilation of the database, we validate and calibrate the model constants against lab-scale experimental data, and finally we compare the current methodology

with state-of-the-art industrial practices.

2. Methodology

We generate nonlinear kinematics for a large number of extreme sea states, with combinations of significant wave heights H_S , peak periods T_P and water depths h , that are representative for storms in offshore locations.

With these three parameters and the constant gravity g , it is possible to define two nondimensional numbers that completely define the parameter space

$$h^* = \frac{h}{gT_P^2} \quad (1)$$

$$H_S^* = \frac{H_S}{gT_P^2} \quad (2)$$

Following standard practices [11], the peak enhancement factor γ was

$$\gamma = \begin{cases} 5 & T_P/\sqrt{H_S} \leq 3.6 \\ \exp(5.75 - 1.15T_P/\sqrt{H_S}) & 3.6 < T_P/\sqrt{H_S} \leq 5 \\ 1 & 5 < T_P/\sqrt{H_S} \end{cases} \quad (3)$$

To generate the nonlinear kinematics, we create a two-dimensional (2D) computational domain on which we execute the nonlinear potential flow model OceanWave3D [7]. The domain is specified in Figure 1.

In order to generate independent runs, we choose 8 different values of the nondimensional number H_S^* , see Table 1. For each sea state, different realizations are run. For each realization, a different set of random phases in the interval $[0, 2\pi)$ is sampled from a uniform distribution and assigned to each wave component of the generated JONSWAP spectrum. A total of 67 different surface elevation signals were imposed in a relaxation zone at the offshore boundary of the OW3D domain. As each simulation ran, waves propagated from the deep offshore region to the shallow onshore region of the domain. To collect results at different nondimensional depths h^* , the wave kinematics were sampled at the shallow part of the domain along vertical lines between the bed and the free surface at 144 different x -locations. In Figure 1, each sampling location is highlighted with a black line. Further details on the computational domain and on the solver are given in the following sections.

	H_S	T_P	γ	H_S/gT_P^2	N_R
1	4.5	15.15	1	$2.0 \cdot 10^{-3}$	9
2	6.76	15.15	1	$3.0 \cdot 10^{-3}$	9
3	9.01	15.15	1	$4.0 \cdot 10^{-3}$	7
4	11.26	15.15	1.75	$5.0 \cdot 10^{-3}$	8
5	13.51	15.15	2.75	$6.0 \cdot 10^{-3}$	9
6	15.77	15.15	3.9	$7.0 \cdot 10^{-3}$	8
7	18.02	15.15	5	$8.0 \cdot 10^{-3}$	10
8	22.52	15.15	5	$1.0 \cdot 10^{-2}$	7
Total					67

Table 1: Sea states input in the computational domain. N_R is the number of realizations that were run for each sea state.

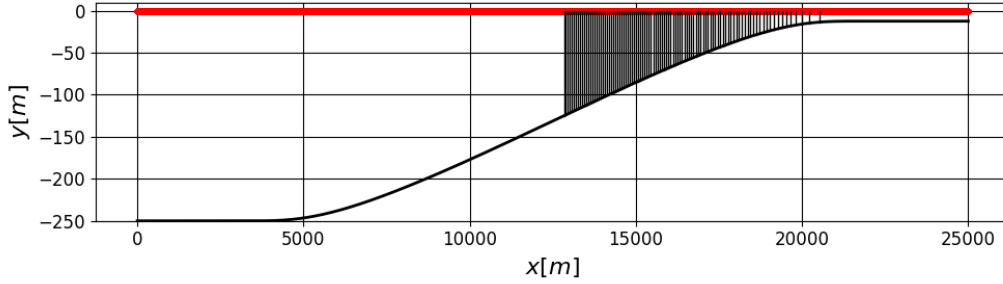


Figure 1: Computational domain. The red line indicates the still water line. The vertical black lines indicate the locations at which the kinematics was sampled. The thick black line is the sea bottom.

2.1. The nonlinear potential solver OceanWave3D

The OceanWave3D flow model was developed at DTU as a robust and fast fully-nonlinear potential solver [7]. The code solves the Laplace equation by a high-order finite difference method, taking into account the fully nonlinear free surface boundary kinematic and dynamic conditions.

$$\partial_t \eta = -\nabla \eta \cdot \nabla \tilde{\phi} + \tilde{w}(1 + \nabla \eta \cdot \nabla \eta) \quad (4)$$

$$\partial_t \tilde{\phi} = -g\eta - \frac{1}{2}(\nabla \tilde{\phi} \cdot \nabla \tilde{\phi} - \tilde{w}^2(1 + \nabla \eta \cdot \nabla \eta)), \quad (5)$$

where $\partial_x \psi = \partial \psi / \partial x$, and the tilde stands for quantities evaluated at the free surface. In the above equation, η is the free surface elevation, ϕ is the fluid scalar potential, t is time, and (u, v, w) are the components of the velocity vector in the (x, y, z) directions.

The velocity potential satisfies

$$\phi = \tilde{\phi}, \quad z = \eta \quad (6)$$

$$\nabla^2 \phi + \partial_{zz} \phi = 0, \quad -h \leq z < \eta \quad (7)$$

$$\partial_z \phi + \nabla h \cdot \nabla \phi = 0, \quad z = -h \quad (8)$$

Equation 8 is the condition of impermeability of the seabed.

In the OceanWave3D formulation, the (x, y, z) coordinate system is changed to a (x, y, σ) system, which makes it possible to solve the problem in a time-invariant grid

$$\sigma \equiv \frac{z + h(x, y)}{\eta(x, y, t) + h(x, y)} \in [0, 1] \quad (9)$$

Once the potential is solved for, the velocity is obtained via differentiation in different directions. Further details are available in Engsig-Karup et al. [7].

2.1.1. The numerical domain

The domain is discretized by $(N_x, N_y, N_z) = (16385, 1, 17)$ points. The domain is $L_x = 25 \cdot 10^3 [m]$ long, which resulted in a grid size of $\Delta x = 1.53 [m]$. The depth L_z varies from $h = 250 [m]$ to $h = 12.5 [m]$ at the outlet.

The average slope is 1/100, with a tangent hyperbolic shape, as defined by

$$x^* = \frac{x - L_{\text{in}}}{L_{\text{out}} - L_{\text{in}}} - \frac{1}{2}, x \in [0, L_x] \quad (10)$$

$$h(x) = \begin{cases} h_{\text{in}} & x^* \leq -\frac{1}{2} \\ h_{\text{in}} - \frac{1}{2}(h_{\text{in}} - h_{\text{out}}) \left(1 + \tanh \frac{\sin(\pi x^*)}{1 - 4x^{*2}} \right), & -\frac{1}{2} < x^* \leq \frac{1}{2} \\ h_{\text{out}} & x^* > \frac{1}{2} \end{cases} \quad (11)$$

The wave generation zone is positioned between $x = 0$ and $x = L_{\text{in}}$, while the wave absorption zone is between $x = L_{\text{out}}$ and $x = L_x$. For the current domain, the following set of parameters is used

$$\begin{aligned} h_{\text{in}} &= 250.0[m], h_{\text{out}} = 12.5[m] \\ L_{\text{in}} &= 2.5 \cdot 10^3[m], L_{\text{out}} = 22.5 \cdot 10^3[m], L_x = 25.0 \cdot 10^3[m] \end{aligned}$$

The spectrum high-cut (hc) frequency is set at $f_{\text{hc}} = 1/3[\text{Hz}]$ for all of the performed simulations, corresponding to a wave with linear wavelength of $L_{\text{hc}} = 14.04[m]$ and $kh_{\text{hc}} = 110.39$. Thus, the shortest wave in the spectrum is resolved with a minimum of $n_x = 9$ grid points in the x -direction. For every grid, we indicate with N_i the total number of points in the direction i , and with n_i the number of points per wavelength in the direction i . The input spectrum is discretized into 2^{19} components in the frequency axis, to achieve a $\Delta t = 0.07[\text{s}]$, which guarantees a return time of 10 hours. Each simulation is run for 8 hours of physical time. The first 1.7 hours are left out to allow the shortest generated wave in the linear spectrum to travel to the last of the sampling locations.

2.1.2. Wave generation and wave absorption strategy

OceanWave3D implements different wave generation techniques. Among others, it is possible to impose linear irregular waves in a relaxation zone or to generate waves by enforcing a boundary flux. To generate the database, a $L_{\text{in}} = 2500[m]$ long wave generation zone is employed. Linear wave theory is

used to calculate the prescribed linear solution for all of the sea states specified in Table 1. At the outlet of the domain, a numerical beach absorbs the outgoing waves. OceanWave3D implements a linear friction damping applied to the tangential velocity, following the strategy by Clamond et al. [12], which dissipates energy and minimizes reflections. In the current computations, the wave absorption zone is 2500[m] long.

2.1.3. Breaking filter

To prevent instabilities arising from near-breaking waves, OceanWave3D has a simple breaking filter that smooths the free surface when the downward Lagrangian particle acceleration Dw/Dt overcomes a certain fraction β of the gravitational acceleration g . If the downward acceleration is lower than the threshold at a domain location, the solver smooths a 10-point region centered at the point with a 3-point filter, where the i^{th} free surface elevation is computed as

$$\eta_i = 0.25\eta_{i-1} + 0.5\eta_i + 0.25\eta_{i+1}. \quad (12)$$

The parameter β is typically $\beta \in [0.3, 0.7]$. Physically, if a particle at the free surface is falling with an acceleration of g it is in free fall, and therefore the wave is breaking. From previous studies, we observed that a value of $\beta = 0.5$ usually gives good agreement with the experiments [13, 14]. An investigation into the choice of the β factor is given in section 4.

2.1.4. Grid convergence study

In Engsig-Karup et al. [7], a detailed discussion of the accuracy and convergence of the solver is provided. The authors investigated the effect of the number of vertical points N_z on the dispersion error for a linear wave, in combination with the size of the differentiation scheme r , the clustering of the grid towards the surface and the number of grid points per wavelength n_x .

When $r = 7$ and $N_z = 17$ clustered points are used in the vertical direction, Engsig-Karup et al. show that the phase error on a linear wave is close to zero up to a $kh = 30.0$, provided $n_x = 9$ points per wavelength are employed in the horizontal direction. They conclude that using a clustered grid in the vertical direction brings great advantages over an evenly spaced grid in terms of convergence, mainly when a higher-order scheme is used for the differentiation.

A similar conclusion was drawn by Schløer [15], who performed a thorough analysis of the necessary discretization to describe an irregular sea state on a shoaling domain, similar to the one that was analyzed in the current work. The shortest wave in their computational domain had a frequency of $f = 0.50[\text{Hz}]$ and a wavelength of $\lambda = 6.25[\text{m}]$, which led to a $kh \approx 80$ in the deepest side of the domain. They found that a grid with $N_z = 17$ points in the vertical direction and $n_x = 8$ was necessary to achieve a good convergence of the simulation, both for the phase and the amplitude dispersion. Based on the above discussion, $N_x = 16835$ grid points and $N_z = 17$ were chosen for the production grid of the current simulations.

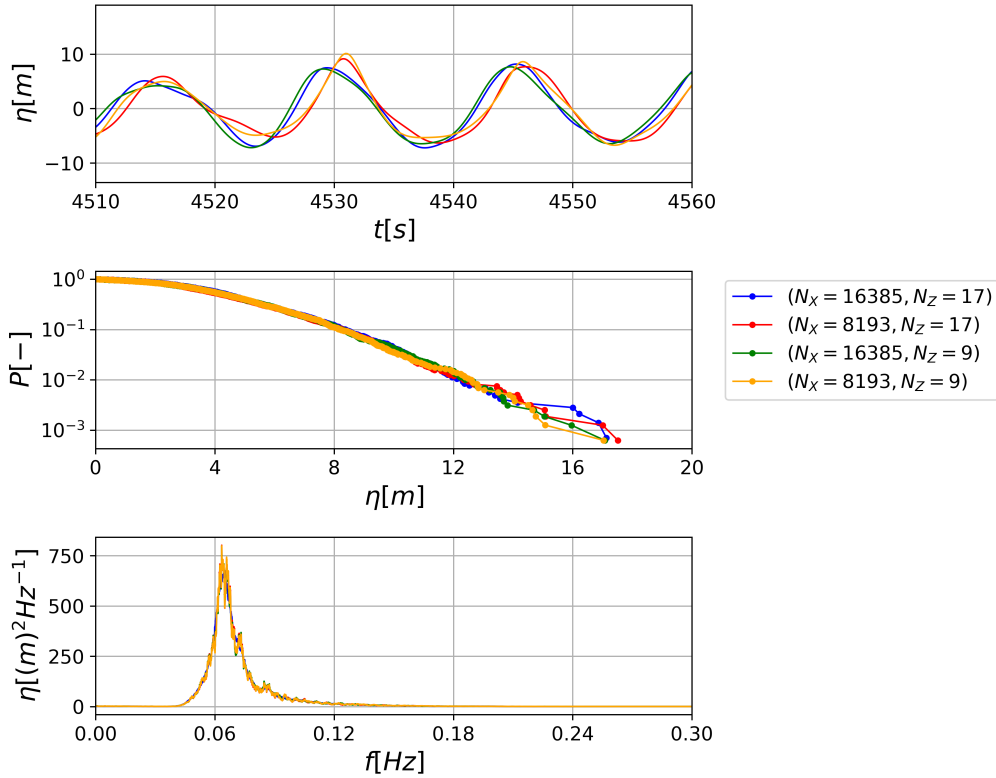


Figure 2: Grid dependency study. $H_S = 15.77[\text{m}]$, $T_P = 15.15[\text{s}]$, $\gamma = 3.9$. Time series sampled at $h = 75.0[\text{m}]$ and at $x = 15 \cdot 10^3[\text{m}]$.

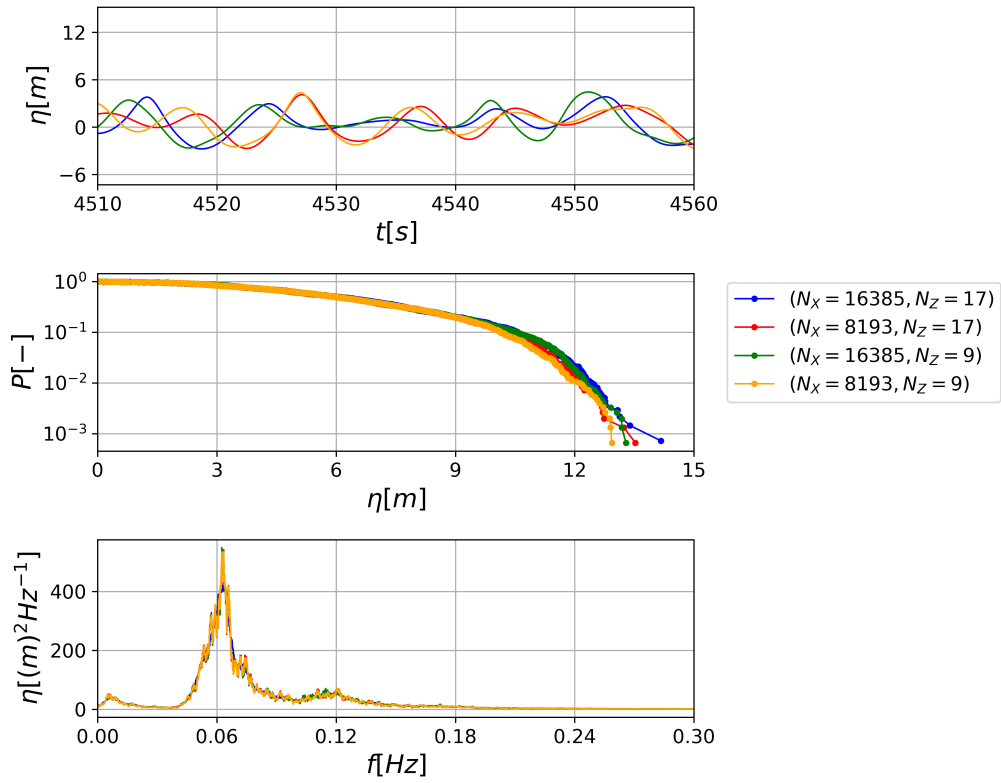


Figure 3: Grid dependency study. $H_S = 15.77[m]$, $T_P = 15.15[s]$, $\gamma = 3.9$. Time series sampled at $h = 25.0[m]$ and at $x = 18.9 \cdot 10^3[m]$.

As a further check, we perform simulations with different grid discretizations on sea state 6 in Table 1, keeping all the other parameters constant and using a breaking factor $\beta = 0.5$. In Figure 2, we can observe the effect of halving the grid resolution in the x -direction (red), in the z -direction (green), and in the x - and z -direction together (orange). The time series was sampled at $x = 15500[m]$, at a depth of $h = 75.0[m]$, in a region that is characterized by a light breaking, see Figure 4. The power spectral densities

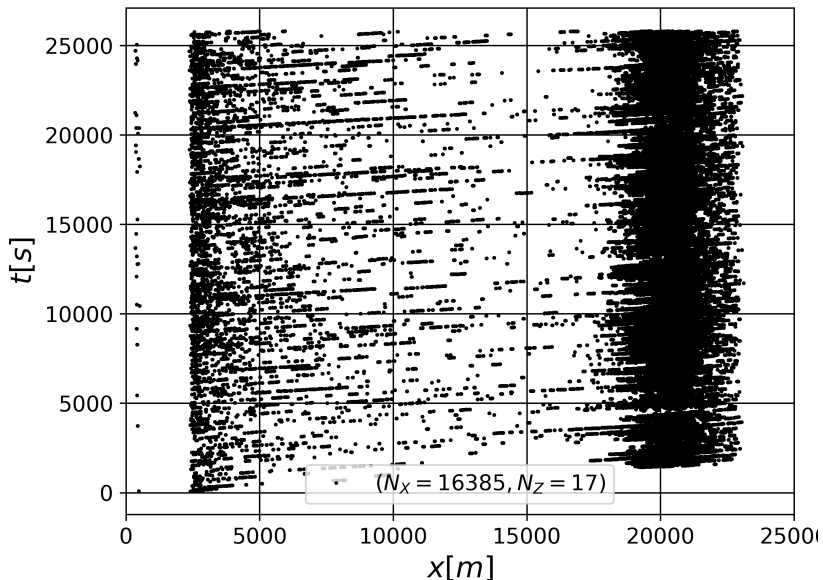


Figure 4: The black dots represent the locations and time instants at which the breaking filter ($\beta = 0.5$) is active, for sea state 6 in Table 1.

are not affected by the change in discretization, while the peak statistics are. Halving the number of grid points either in the x - or in the z -direction brings along a 3% reduction in the crest heights for a probability level $P < 3 \cdot 10^{-2}$, independent of the x -discretization.

In the subset of the time signal plotted in the top subfigure, the discretization in the x direction affects the phase of the waves. Curves obtained with the same x -wise discretizations seem to be in phase with each other (red and orange; green and blue). The z -wise discretization seems to impact on the sharpness of the peaks. Indeed, some phase error on the wavelengths above $kh = 10.0$ is expected when $N_z = 9$ (see figure 8 of Engsig-Karup et al. [7]), which can reduce or enhance local crest heights by changing the time at

which wave components superimpose. However, since the crest statistics are to a large extent unchanged, and since the chosen resolution is found here to be conservative, we conclude that reducing the discretization has a negligible impact on the amplitude errors of these small waves.

In Figure 3, which was generated with data sampled at $x = 18.9 \cdot 10^3[m]$ at a depth of $h = 25.0[m]$, a similar tendency is visible. In this zone heavy breaking is occurring, cf. Figure 4. The top subplot confirms that the wave crests for signals with the same x -wise discretization are synchronized. In the center subplot, a deviation between the two sets of simulations with $N_x = 16385$ and $N_x = 8193$ is visible for crests with low exceedance probability ($P < 1 \cdot 10^{-2}$). This suggests that reducing the x -wise discretization modifies the behavior of the breaking filter, which is overall more active and subtracts more energy. However changing the discretization has a negligible effect on the height of the largest crest. We conclude that our simulations with ($N_x = 16385, N_z = 17$) have converged to a satisfactory level.

3. Application for load computation

3.1. Visualization of the Database

In Figure 5, all the 9648 sampled points are represented in terms of their H_S^* and h^* .

3.2. Extraction of kinematics and generalization via Froude scaling

We denote as $(H_{S,0}, T_{P,0}, h_0)$ the combination of sea state and depth for which kinematics need to be produced. This tuple uniquely identifies a point in the (h^*, H_S^*) plane. It is possible to extract from the database a number of realizations that are nondimensionally identical to the required sea state.

In the nondimensional plane (h^*, H_S^*) , the distance Δ of the i^{th} sea state to the sea state of interest $(h_0^*, H_{S,0}^*)$ can be calculated as:

$$\Delta_i = \sqrt{(h_0^* - h_i^*)^2 + (H_{S,0}^* - H_{S,i}^*)^2} \quad (13)$$

According to Δ_i , we select the N database points closest to the sea state of interest, where typically $N = 5$. Only one realization per actual run of the solver is chosen since we are only interested in statistically independent simulations.

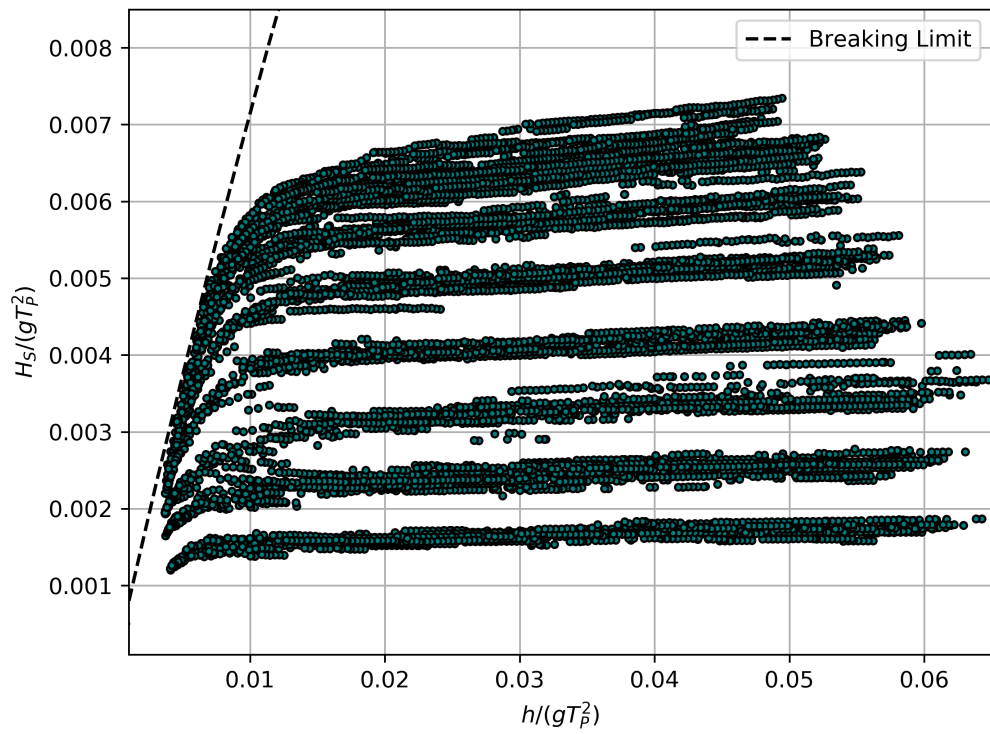


Figure 5: Realizations of the experiments collected in the database. The black dashed line is the theoretical breaking limit for regular waves.

-	$H_S[m]$	$T_P[s]$	γ	$L_x[m]$	$h_{in}[m]$	$h_{out}[m]$	$h_{sample}[m]$	$\Delta t[s]$
Original	15.77	15.15	3.9	$25 \cdot 10^3$	250.0	12.5	25.0	0.07
Scaled	10.09	12.12	3.9	$16 \cdot 10^3$	160.0	8.0	16.0	0.056

Table 2: The two sea states and domain configurations used to test the Froude Scaling Hypothesis.

To match the scale of the sea state of interest, we need to compute a factor S_i for each i^{th} sea state, with $i = 1..N$, by taking the ratio of the depth of the database point and the depth of the sea state of interest

$$S = \left(\frac{h_0}{h_i} \right) \quad (14)$$

Once the scaling factor is calculated, the simulated velocity, wave elevation, acceleration time series and time are Froude-scaled via

$$\eta_i^{\text{scaled}}(x, y, t) = \eta_i(x, y, t)S_i \quad (15)$$

$$u_i^{\text{scaled}}(x, y, t) = u_i(x, y, t)S_i^{1/2} \quad (16)$$

$$u_{t,i}^{\text{scaled}}(x, y, t) = u_{t,i}(x, y, t) \quad (17)$$

$$t_i^{\text{scaled}} = t_i S_i^{1/2} \quad (18)$$

3.2.1. Testing of the Froude scaling hypothesis

We verify the appropriateness of the Froude scaling hypotheses by comparing the results of two simulations, one at full scale and one in a scaled domain. The full scale simulation was performed on the domain in section 2.1.1. The second simulation was performed on a smaller domain, scaled by a geometrical factor $S = 0.64$. The parameters for the scaled simulation are in Table 2. The significant wave height and peak periods were also scaled to $H_S = 10.09[m]$ and $T_P = 12.12[s]$, while the peak enhancement factor was the same, $\gamma = 3.9$. The scaled spectrum was cut at the same nondimensional frequency $kh_{in} = 114.39$. The number of grid points was also equal, with $(N_x, N_y, N_z) = (16385, 1, 17)$, while the time step for the scaled simulation was reduced to $\Delta t = 0.056[s]$.

In Figure 6 we plot the statistics for a free surface elevation signal of 3 hours, sampled at $x = 12.8 \cdot 10^3[m]$, at a depth of $h = 125.0[m]$. When the

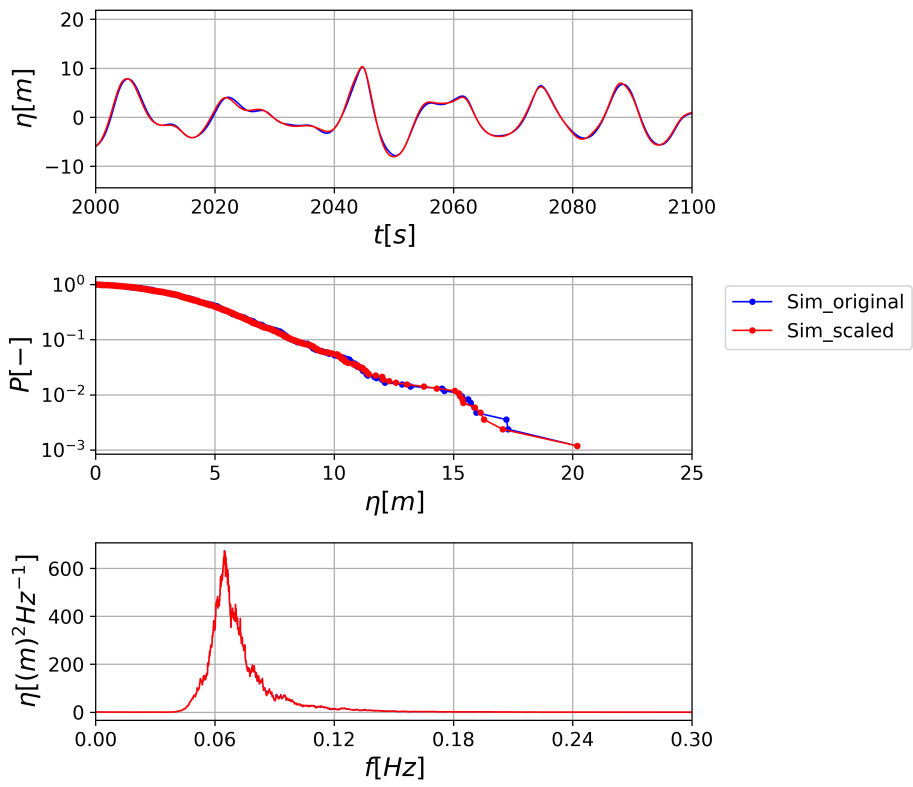


Figure 6: Comparison between the original and the scaled computation.

simulation in the small domain is scaled up, the peak exceedance probabilities of the free surface elevation are the same, with some minor discrepancies on the peak values. The same is true for the power spectral densities, which accurately match. Due to the successful deterministic comparison of the surface elevation, we infer that the kinematics behave accordingly. We conclude that the results sampled in a particular domain can be Froude scaled without loss of generality.

3.3. The force models

Once the wave kinematics are known, according to Rainey [16], the horizontal sectional force f_x on the cylinder is computed as

$$f_x = \frac{1}{2}\rho C_D D u |u| + \rho(1 + C_m)\pi R^2 \frac{du}{dt} \quad (19)$$

where ρ is the fluid density, C_D is the drag coefficient, C_m is the added mass coefficient, $R = D/2$ is the cylinder radius, and du/dt is the total (material) derivative of the streamwise velocity.

The horizontal axial divergence distributed force is computed by

$$f_{x,ad} = \rho\pi R^2 C_m w_z u \quad (20)$$

where $w_z = \partial w / \partial z$. This force accounts for the fact that although the cylinder is slender in the horizontal direction, it is not slender in the vertical direction with respect to the wavelength. The force at the monopile base is obtained by depth-integrating the distributed force contributions from the bottom of the monopile $z = -h$ to the time-varying surface elevation $z = \eta(t)$. The distributed force from Equation 19 and 20 agrees with the recently published force model by Kristiansen and Faltinsen [17].

A point force is added at the intersection between the surface and the cylinder, to take into account for the change of fluid kinetic energy which happens when the wet length of the cylinder varies

$$F_\eta = \frac{1}{2}\rho\pi R^2 C_m \eta_x u^2 \quad (21)$$

where $\eta_x = \partial \eta / \partial x$. The Rainey load model is derived on energy conservation grounds only, and does not make any assumptions on the incoming

waves, except for the fact that the cylinder is slender and does not modify the wave surface, also called the *wavy lid assumption*. While this point force differs from the F^ψ in Kristiansen and Faltinsen [17], a recent study of Suja-Thauvin et al. [18] concluded that the third-harmonic content of the two terms agree for large waves.

To find values for $C_M = C_m + 1 = 2$ and C_D for the smooth steel cylinder, a designer normally relies on recommended practices, as DNV-RP-C205 (see 6-7 and 6-9 in [11]). Generic values for a smooth cylinder at sub-critical Reynolds numbers are $C_m = 1.0$ and $C_D = 1.0$. We discuss our choice of parameters in the results section.

4. Comparison of Numerical and Experimental results

4.1. The DeRisk experiments

The model tests used here for comparison were performed at DHI in 2015 in the framework of the DeRisk project. The experiments aim to reproduce storms with different return times (10 to 1000 years) for two typical North Sea locations ($h = 20[m]$ and $h = 33[m]$ depth). Values in this section are in full scale, which is 50:1 to laboratory scale, except where otherwise indicated. The experimental setup is sketched in Figure 7. The effective length of the basin is reduced by positioning arc-shaped steel wave absorbers in an M-shape, to direct the reflected waves away from the cylinder. To further mitigate wave reflection, crushed stones were arranged on the basin's edges with a slope of 1:5.

The PVC cylinder with a diameter of $D = 7.0[m]$ is positioned 365.0[m] away from the paddles. The cylinder is supported by two force transducers, one at the top and one at the bottom, sampled at a frequency of 178.2[Hz]. The first bending eigenfrequency of the transducers and cylinder assembly is tuned to be far away from the wave spectrum frequencies to reduce the dynamic structural response.

The basin's wave maker is made up of 36 piston-type wave paddles and is capable of generating both 2D and 3D waves. The wave paddle signal for each of the test runs is stored, so that it can be reproduced numerically at a later stage. An array of 5×5 wave gauges is positioned around the cylinder with a full-scale spatial resolution of 10[m]. Five additional wave gauges are located in the space between the wave gauge array and the wave paddle generator. The wave gauge signal is sampled at 12.7[Hz]. A 3D Vectrino velocimeter is

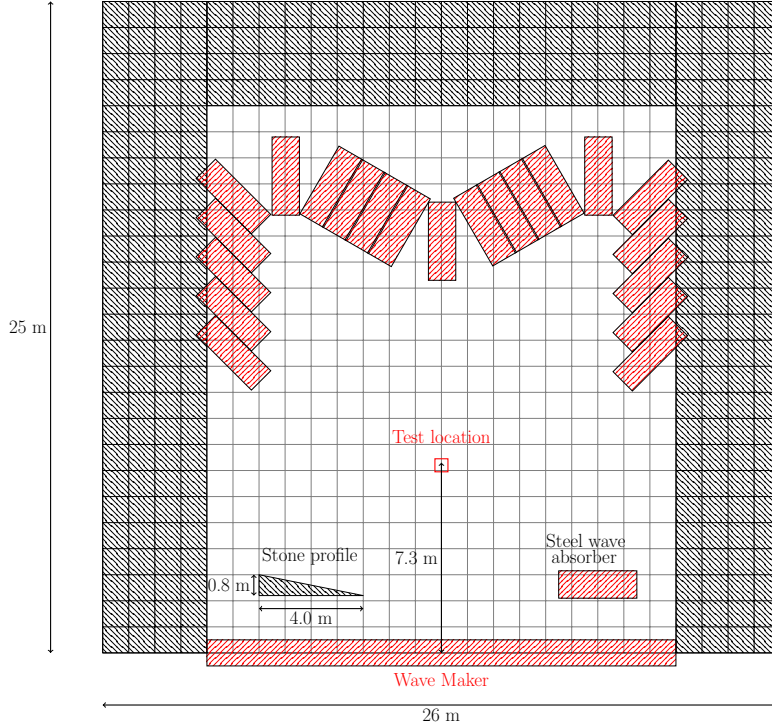


Figure 7: DeRisk experimental setup in model scale, which is 1:50 with respect to full scale. The grid resolution is $1[m] \times 1[m]$. Adapted from Figure 1 in Bredmose et al. [9].

positioned in the wave tank right in front of the cylinder, located at half the wave tank's water depth.

In this work, all the experiments are analyzed, but we only present plots for experiments 11 ($h = 33.0[m]$) and 23 ($h = 20.0[m]$). In these tests, two steep sea states with a 100-year (yr) return period were applied, and we expect the waves to be strongly nonlinear.

4.2. Reproduction of experiments on a flat domain with boundary-flux wave generation

To validate the flow model, we replicate the DeRisk experimental results via OceanWave3D. In a previous study by Schl er et al. [13], experiments 23 and 24 of Table 3 are reproduced deterministically via OceanWave3D by using the experimental wave paddle signal to drive the flux at the numerical wave generation boundary. The numerical domain has a full-scale size of $L_x = 1000.[m]$, a flat bottom with a constant depth of $h = 20.0[m]$, and was

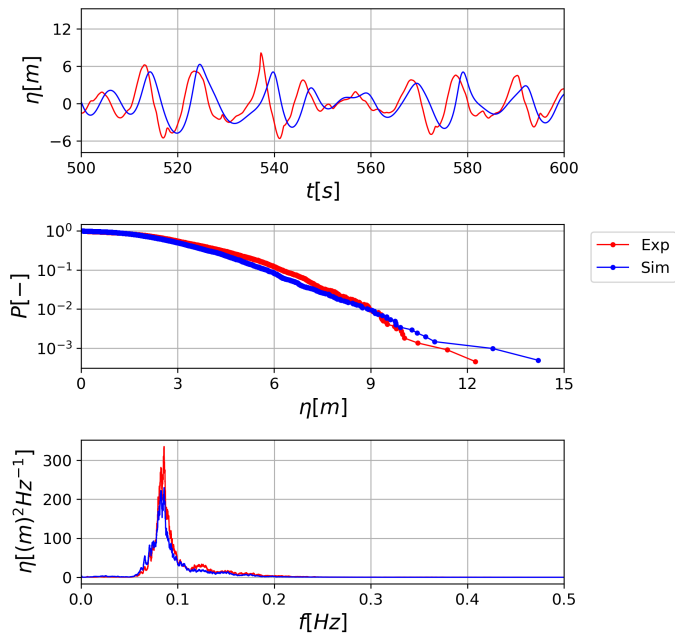
No.	Nominal			Measured			
	H_S	T_P	γ	H_S	T_P	Depth[m]	Return [yr]
1	8.50	13.50	1.53	9.12	12.28	33.00	10
9	7.50	12.00	2.04	7.78	11.16	33.00	10
10	7.50	15.00	1.00	7.36	13.61	33.00	10
11	9.50	12.00	3.57	9.81	11.62	33.00	100
12	9.50	15.00	1.17	9.18	13.61	33.00	100
13	11.00	15.00	1.73	10.26	13.68	33.00	1000
20	5.80	12.00	1.02	6.05	12.10	20.00	10
21	5.80	15.00	1.00	6.16	12.41	20.00	10
22	6.80	12.00	1.58	7.09	12.25	20.00	100
23	6.80	15.00	1.00	7.04	14.06	20.00	100
24	7.50	15.00	1.00	7.65	14.06	20.00	1000
25	5.80	9.00	4.27	6.09	8.82	20.00	1000

Table 3: Experimental tests with long-crested waves. We report both the nominal values, imposed at the boundary and the measured values at the cylinder location.

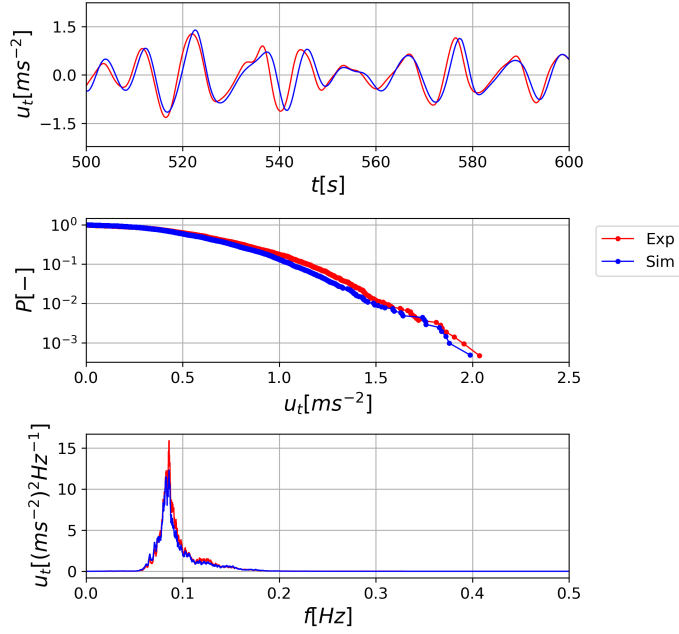
discretized into $(N_x, N_y, N_z) = (201, 1, 15)$ grid points. The distance between the sampling point and the wave generator is $365.0[m]$, as in the experimental domain (see Figure 7). Part of the discrepancy between the measured and the target significant wave height is due to breaking. For the 1000-yr storms, breaking was visually observed right in front of the paddle. However, it is difficult to quantify the amount of energy lost due to the viscous dissipation process.

To calibrate our simulations, we reproduce Experiments 11 and 23 using the same computational domain and grid discretization as in Schløer et al., and we compare numerical and experimental free surface elevation and Eulerian acceleration. The results in Figure 8, relative to the 100-yr storm at depth $h = 33.0[m]$ obtained with $\beta = 0.5$, show a good agreement. The measured energy distribution at higher frequencies ($f > 0.1[Hz]$) is also correctly reproduced for the horizontal Eulerian acceleration, when compared to measurements by the Vectrino sensor positioned at $z = -16.5[m]$, despite what seems like a small ($\approx 0.1[m/s]$) magnitude systematic error in the exceedance probability.

For the 100-yr storm in the $h = 20.0[m]$ depth are in Figure 9, the best agreement between the wave elevation measurements and the simulated free



(a) Plot of 3 hours of the OceanWave3D wave elevation signal, from simulations and experiment 11 in Table 3, $\beta = 0.5$. Good agreement in the power spectrum and in the crest exceedance probability.



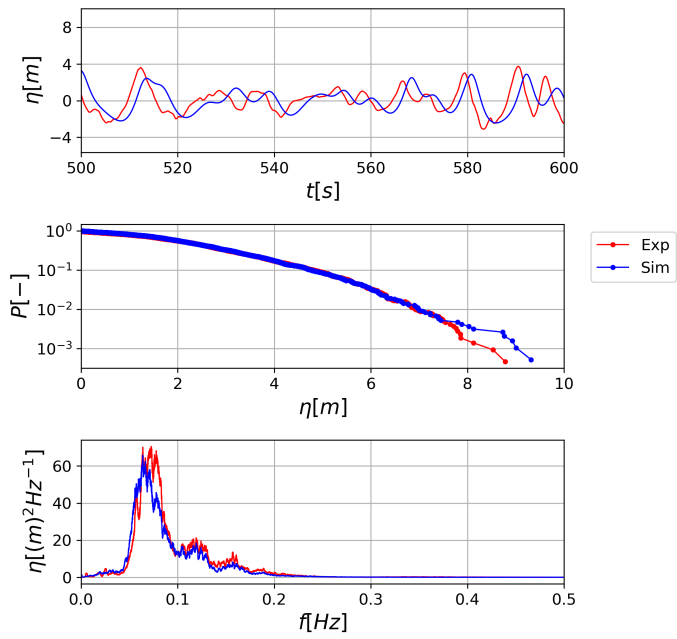
(b) Plot of 3 hours of the OceanWave3D wave horizontal acceleration u_t at $z = -16.5[m]$, from simulations and experiments 11 in Table 3, $\beta = 0.5$.

Figure 8: Test 11 reproduced with the paddle signal.

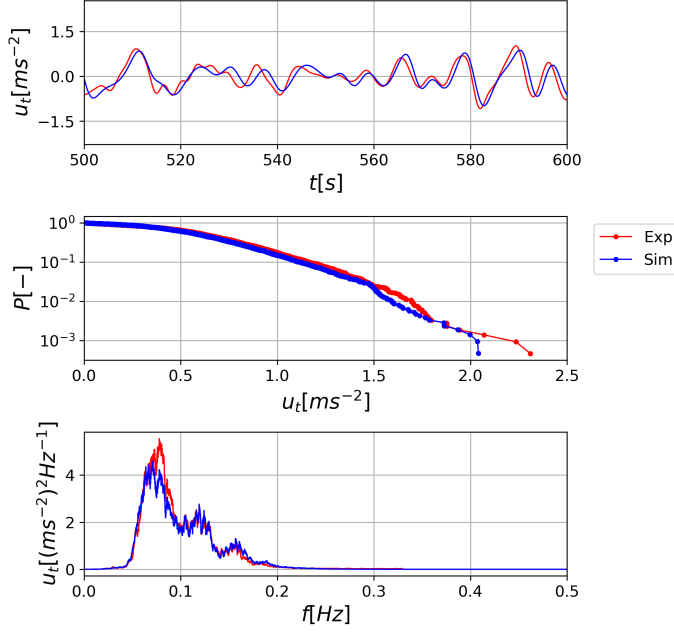
surface elevation power spectral density (PSD) was obtained with $\beta = 0.3$. In particular, the superharmonic peak location and magnitude are very well reproduced, even though some energy is missing in the main peak. The same comparison is in Figure 6 of Schløer et al., which was produced by data sampled on an equivalent computational domain. The peak exceedance probability agrees well down to $P = 2.5 \cdot 10^{-2}$ but diverge for larger values. We regard this as an underestimation of breaking by the simulations.

In Figure 9b, the computed and measured horizontal Eulerian acceleration is compared at $z = -10.0[m]$. The acceleration spectrum is very well estimated by the simulation, even though some energy is missing around the peak frequency. The agreement of the exceedance probability is overall good, although a small deviation is observed for points with probability levels of $P < 1.5 \cdot 10^{-2}$.

We conclude that the potential flow solver with the flux wave generation



(a) Plot of 6 hours of the OceanWave3D wave elevation signal, from simulations and experiment 23 in Table 3, $\beta = 0.3$. The spectra show a good agreement, except close to the spectral peak. The free surface elevation crests statistics deviate for larger waves, probably due to the effect of the breaking filter.



(b) Plot of 6 hours of the OceanWave3D wave horizontal kinematics acceleration u_t at $z = -10.0[m]$, from simulations and experiment 23 in Table 3, $\beta = 0.3$. Good agreement in the spectrum distribution and in the crest exceedance probability.

Figure 9: Test 23 reproduced with the paddle signal. Good agreement both for velocity and acceleration.

reproduces the measurements fairly well, although this approach is quite sensitive to the β factor.

4.3. Reproduction of experiments on a flat domain with waves in a relaxation zone: effect of the wave breaking factor β

We aim to calibrate the optimal breaking factor β for the DeRisk database simulations, where the waves are generated in a relaxation zone rather than with a boundary flux. We thus modify the flat-bed computations in section 4.2 to generate waves by random realizations in a relaxation zone rather than by imposing the boundary flux. The full-scale domain length in these simulations is $L_x = 1350.0[m]$, where the first $350.0[m]$ are used as the buffer zone for wave generation. The domain was discretized into $(N_x, N_y, N_z) =$

(513, 1, 17) grid points. For the two combinations of H_S and T_P of cases 11 and 23 from Table 3, 10 realizations were produced by using 10 different sets of random phases. Each realization was then repeated with three different breaking filter constants, $\beta = [0.3, 0.4, 0.5]$.

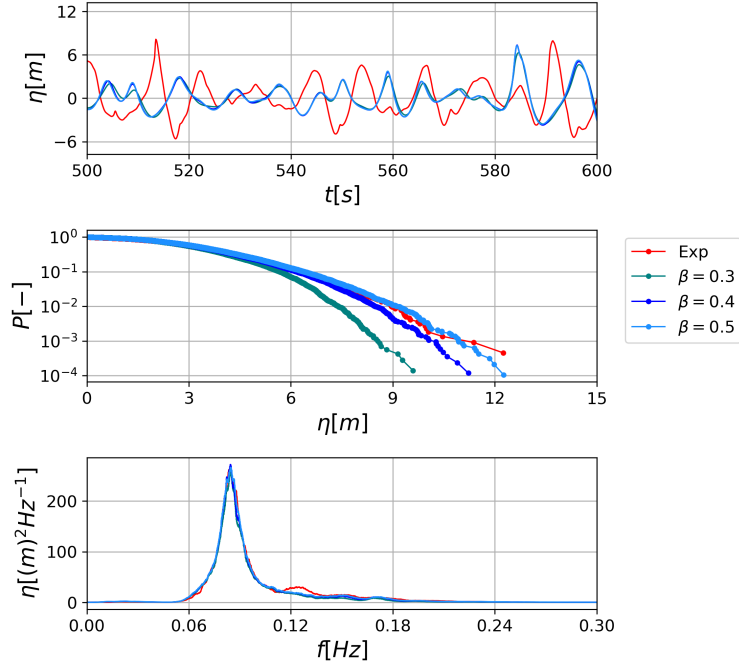
As for Test 11, at $h = 33.0[m]$, in Figure 10a, we notice a very good match between the measured and the simulated wave elevation signal statistics for $\beta = 0.5$. A similar agreement was found in Figure 8a, even though the power spectrum of the boundary flux generated waves showed a better agreement in the super-harmonic region. The breaking factor does not significantly influence the shape of the spectrum, while the surface elevation peak exceedance probability curve shows a marked reduction for $P < 1 \cdot 10^{-1}$ when $\beta = 0.3$.

The statistics of the horizontal Eulerian acceleration, in Figure 10b, agree well for $\beta = 0.5$. The exceedance probability for the kinematic acceleration peaks, though, diverged for probabilities lower than $P = 2 \cdot 10^{-2}$, in contrast to Figure 8b where the tail was well captured. In the case of the statistical comparison, we experience some variability in the tail of the distribution, determined by randomness. The peak exceedance probability for the Eulerian acceleration was less sensitive to β than for the free surface elevation, as the high-frequency components that are mostly affected by the smoothing filter do not penetrate down to $z = -16.5[m]$. For test 11, $\beta = 0.5$ gave the best agreement overall.

In test 23, in Figure 11a, the experimental and numerical secondary peaks in the super-harmonic region of the PSD match both in location and magnitude for $\beta = 0.5$. However, the computations seem to underestimate the magnitude of the main spectral peak, as in Figure 9a. The exceedance probability for $\beta = 0.3$ underestimates the crest height, in contrast to Figure 9a. This suggests that the wave generation in a relaxation zone led to an overall larger amount of breaking, providing a better agreement for a less aggressive breaking constant of $\beta = 0.5$.

The statistics of the streamwise Eulerian acceleration for $\beta = 0.5$ agree well with the experimental ones (see Figure 11b). The main spectral peak of the PSD is weaker than the experimental one and the secondary peak at $f = 0.16[Hz]$ is overestimated. These super-harmonic peaks are due to free waves generated at the inlet boundary and are therefore sensitive to the wave generator type. This aspect will be the subject of a follow-up paper. We expect a less accurate agreement when the wave generation is distributed in a buffer zone rather than concentrated into a boundary flux. The computed peak exceedance probability reproduced the experiments with an acceptable

accuracy down to $P = 3 \cdot 10^{-3}$, despite a small positive bias for $\beta = 0.5$. We conclude that $\beta = 0.5$ again returns the best agreement with the experiments.

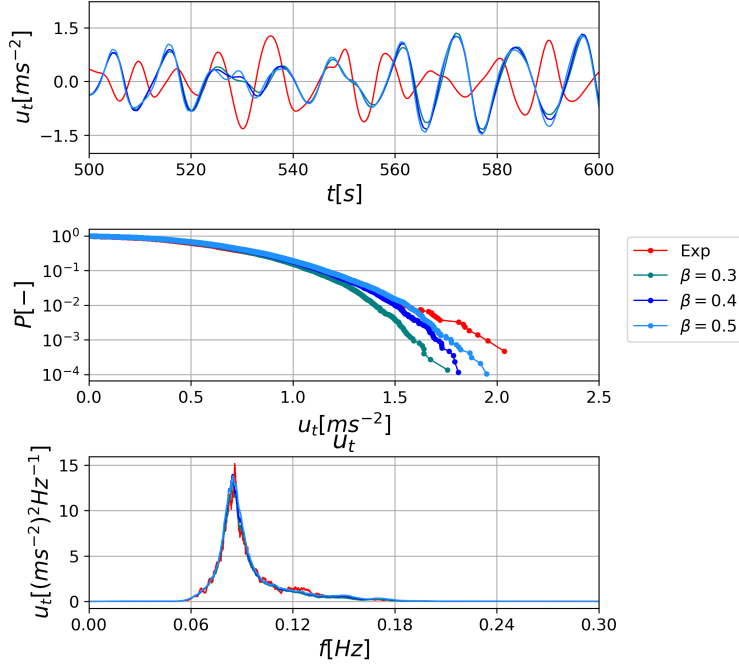


(a) Case 11, 100-yr storm, $h = 33.0[m]$, with $\beta = [0.3, 0.4, 0.5]$. Surface elevation.

The value $\beta = 0.5$ is not in agreement with the suggestions in Schlør et al. [13], which suggested $\beta = 0.3$ for unidirectional waves. We believe this difference is justified by the different wave generation technique. In the Table 4, we collect the optimal β values for all the analyzed cases. We find that $\beta = 0.5$ works well across the full range of the investigated h/gT_P^2 and H_S/gT_P^2 .

4.3.1. Force computations and calibration of the force coefficients

The kinematics database's purpose is to provide a reliable source of extreme wave kinematics. The choice of the mass and inertia coefficients are left to the user of the database. The choice of C_M and C_D for industrial applications is usually based on best practices documents [11]. Another well-cited theory is the asymptotic theory from Bearman et al. [19], which computes

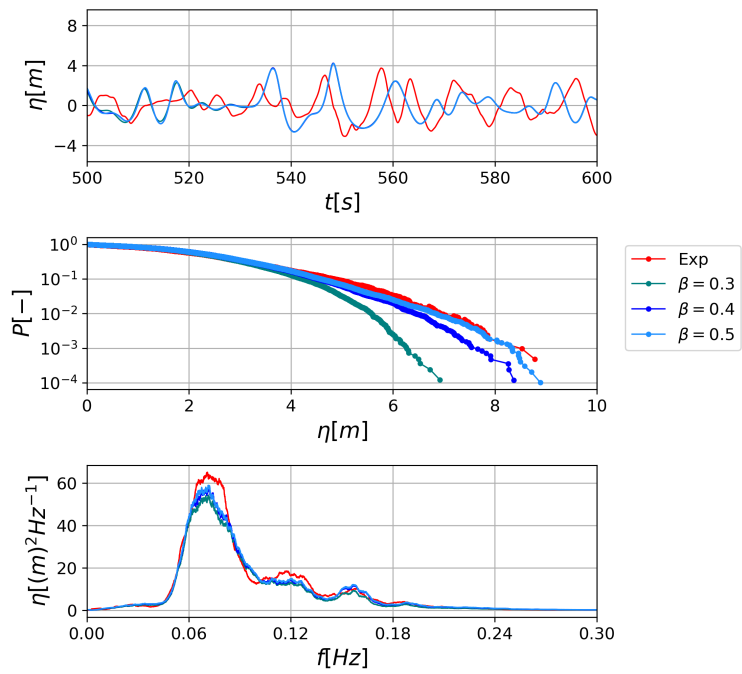


(b) Case 11, 100-yr storm, $h = 33.0[m]$, with $\beta = [0.3, 0.4, 0.5]$. Horizontal Eulerian acceleration at $z = -h/2$.

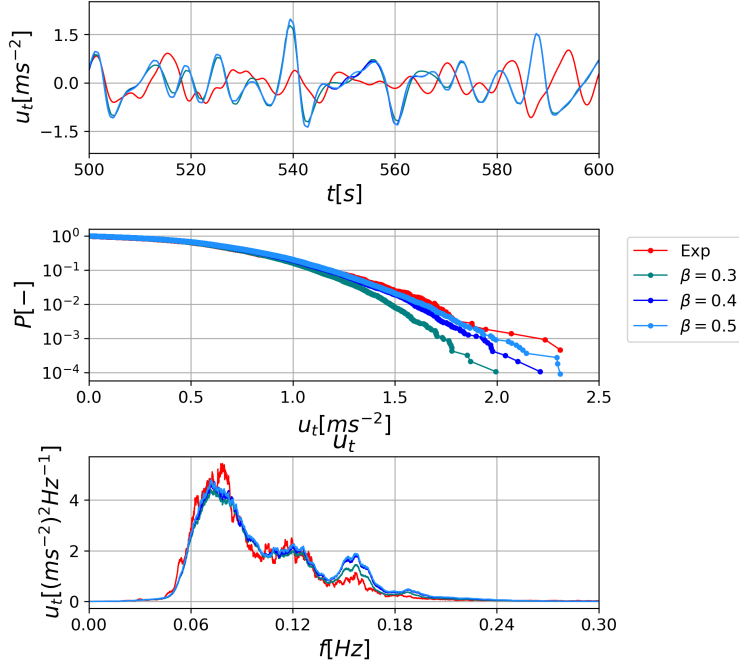
Figure 10: Case 11: comparison with the flatbed database.

the 2D theoretical values of C_M and C_D for low Keulegan-Carpenter numbers ($KC \rightarrow 0$). Longoria et al. [20] used an oscillatory irregular flow on a submerged cylinder in a water tunnel to investigate the effect of irregular waves on the mass and drag coefficients of circular cylinders. For a ratio of $Re/KC \approx 2300$, they report a $C_M = 1.6$ and a $C_D = 1.0$ for a $KC \approx 3.0$. Some authors correct the values of the mass and drag coefficient on a per-wave basis [21], or according to the depth below the free surface where the flow is usually more inertia-dominated.

When experimental data are available, it is possible to find the C_M and C_D coefficients that describe the measured forces best and facilitate the comparison of the load statistics. Ghadirian and Bredmose [14] used a least-square fit to compute the C_M and C_D that would result in the best fit between the



(a) Case 23, 100-yr storm $h = 20.0$ [m], with $\beta = [0.3, 0.4, 0.5]$. Surface elevation.



(b) Case 23, 100-yr storm, $h = 20.0[m]$, with $\beta = [0.3, 0.4, 0.5]$. Horizontal Eulerian acceleration at $z = -h/2$.

Figure 11: Case 23: comparison with the flat-bed database.

measured and the simulated force time series. In this paper, we follow a similar approach. As the low KC number at the free surface suggests that the process is inertia-dominated for the whole cylinder, we expect the main population of the force crest distribution to depend linearly on the mass coefficient C_M . We also expect the drag coefficient C_D to play an important role only for the large force events, in the tail of the force crest distribution. Therefore, we scale the mass coefficient C_M to match the standard deviation of the experimental force signals.

To compute the optimal mass coefficient, we use the following procedure. First, we compute the horizontal force time series using $C_M = 2.0$ as first-guess value, with $C_D = 1.0$. Then we derive a correction factor χ as the ratio between the standard deviation of the experimental force signal σ_F^{exp} and the

Test N.	h/gT_P^2	H_S/gT_P^2	β	C_M^*	KC
1	$2.23 \cdot 10^{-2}$	$6.17 \cdot 10^{-3}$	0.5	1.70	2.89
9	$2.70 \cdot 10^{-2}$	$6.37 \cdot 10^{-3}$	0.5	1.72	2.44
10	$1.82 \cdot 10^{-2}$	$4.05 \cdot 10^{-3}$	0.5	1.71	2.37
11	$2.49 \cdot 10^{-2}$	$7.41 \cdot 10^{-3}$	0.5	1.74	2.93
12	$1.82 \cdot 10^{-2}$	$5.05 \cdot 10^{-3}$	0.5	1.71	2.90
13	$1.80 \cdot 10^{-2}$	$5.59 \cdot 10^{-3}$	0.5	1.84	3.56
20	$1.39 \cdot 10^{-2}$	$4.21 \cdot 10^{-3}$	0.5	1.75	2.21
21	$1.32 \cdot 10^{-2}$	$4.08 \cdot 10^{-3}$	0.5	1.73	2.31
22	$1.36 \cdot 10^{-2}$	$4.82 \cdot 10^{-3}$	0.5	1.75	2.53
23	$1.03 \cdot 10^{-2}$	$3.63 \cdot 10^{-3}$	0.5	1.64	2.89
24	$1.03 \cdot 10^{-2}$	$3.95 \cdot 10^{-3}$	0.5	1.70	3.04
25	$2.62 \cdot 10^{-2}$	$7.98 \cdot 10^{-3}$	0.5	1.66	1.73
$\bar{\square}$				1.72	
σ_{\square}				0.048	

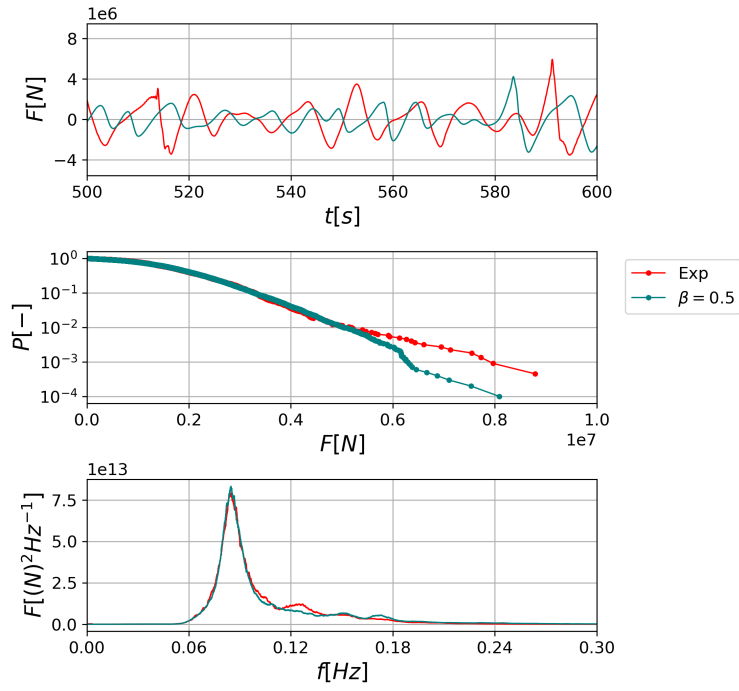
Table 4: Optimal breaking factors. In general, $\beta = 0.5$ was found to give the best agreement. KC was based on the standard deviation of the streamwise surface velocity $KC = \sigma_{u|_{z=\eta}} DT^{-1}$.

standard deviation of the experimental force signal σ_F^{sim} , by which we find a new mass coefficient $C_M^* = C_M \cdot \chi$. We finally rerun the force computation.

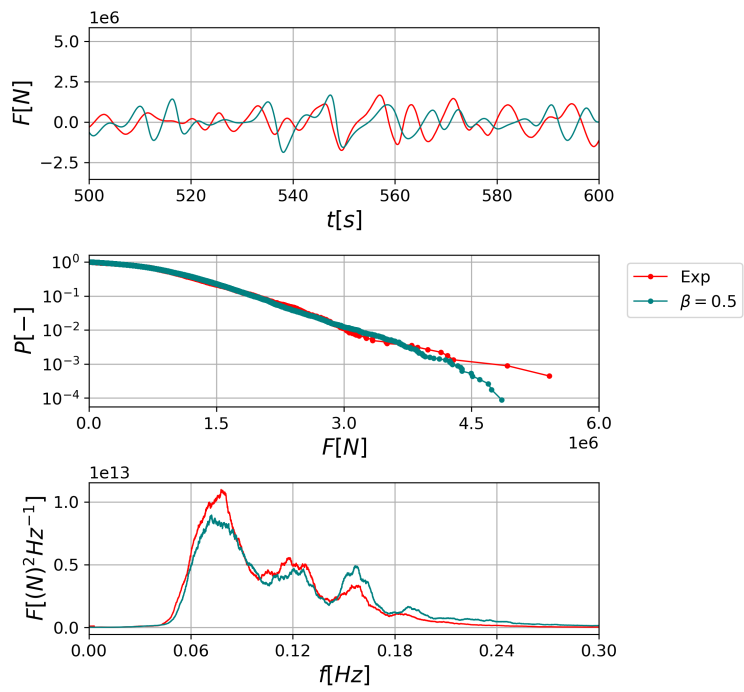
We use a constant $C_D = 1.0$, following the suggestion of Schløer et al. [13]. In principle, it is possible to modify the C_D until a good agreement is found in the tail of the force crest exceedance probability plot. However, some extreme force peaks ($P < 2 \cdot 10^{-2}$) are associated with slamming forces by breaking waves. Since the current model does not include any slamming contribution, compensating by enhancing the drag coefficient would lead to an unphysical overestimation of the drag force.

We obtain a list of corrected C_M^* values as summarized in Table 4. The investigations of Longoria et al. [20] predicted a $C_M \in [1.6, 1.8]$, comparable with the current findings. This approach for finding C_M was rather insensitive to the choice of the drag coefficient C_D . When recomputing the mass coefficients with a lower drag coefficient, closer to the value suggested by Longoria et al. ($C_D = 0.5$), we obtained very similar mass coefficients, with a maximum deviation of 5% from the values in Table 4.

For test 11, in Figure 12a, a very good correlation on the peak forces for



(a) Case 11, 100-yr at $h = 33.0$ [m]. Corrected C_M and C_D .



(b) Case 23, 100-yr at $h = 20.0$ [m]. Corrected C_M and C_D .

Figure 12: Force computations for case 11 and 23.

up to $P \geq 1.0 \cdot 10^{-2}$ is found. In the tail of the distribution, the simulations underestimate the experimental force. Part of this discrepancy is due to the absence of a slamming load model in the force computations. Pierella et al. [22] showed that coupling a slamming force model to the database allows reconstructing the extreme events with greater accuracy. In the region between $0.1[Hz]$ and $0.2[Hz]$, we observe some secondary peaks in the experimental force spectrum. As above mentioned, this is believed to be the effect of free waves induced at the linear generation boundary. For test 23, in Figure 12b, a similarly good agreement is achieved in the main population of the force crest peak distribution, although the extreme events are better reproduced.

5. Ultimate Load States computation: Current approach versus industrial standard procedures

We compare the DeRisk database methodology with the Embedded stream function (ESF) method from IEC-61400-1 [1], with the Wi-Fi JIP methodologies [23], and with linear and Second-Order irregular waves from Sharma and Dean [24].

5.1. DeRisk database

The procedure to extract the kinematics from the DeRisk database is outlined in section 3. To compute the horizontal force for the different experiments, we use the experiment-specific mass coefficient C_M in Table 4, a drag coefficient of $C_D = 1.0$, and a fluid density of $\rho = 1025.0[kg \cdot m^{-3}]$.

5.2. Embedded stream function

The methodology consists of embedding a nonlinear wave in a linear background realization. At the embedment time t_0 , the kinematics of a linear sea state and of a stream function wave with period T are blended according to a function $g(t) \in [0, 1]$, where $g(t) = 0$ for $t \leq T/2 - t_0$ and $t \geq T/2 + t_0$, and $g(t) = 1$ for $t = t_0$. The force is computed according to the new kinematics, and the response of the structure is simulated to extract the largest load.

This method has three main parameters: the embedment time t_0 , the period of the stream function wave T and the height of the stream function wave H . Depending on their combination, we can identify two main embedment strategies from the literature.

In the *hard embedment* several stream function waves are generated by using

$$H = 1.86H_{S,50}$$

$$11.1\sqrt{(H_S/g)} \leq T \leq 14.3\sqrt{(H_S/g)}$$

where $H_{S,50}$ is the significant wave height for a sea state with 50-yr return time. They are subsequently embedded in a random time instant t_0 in the background regular wave realization, which is usually 3-hr or 1-hr long. When analyzing a stiff structure, a single regular stream function wave can be used. This methodology does not retain the randomness in the height of the largest wave in a realization, which is decided a priori based on the Rayleigh distribution. The constrained wave methodology has further limitations when a flexible structures is analyzed. In this case, the stochastic nature of the load history is important as the static and dynamic loads can freely combine, and the maximum load on the structure does not necessarily happen when the largest wave passes by. This shortcoming is partially addressed by the *soft embedment* methodology, where the largest wave of the realization is suitably replaced by a nonlinear stream function wave [25, 26]. In this work, we consider a stiff cylinder and hard-embed one single cycle of a regular stream function wave with three different periods T in the aforementioned interval and $H = 1.86H_S$.

5.3. The WiFi industry project

The WiFi Joint Industry Project (JIP) [23] provides a method to compute the extreme force with a probability of occurrence of 1/1000 in a 1-hr sea state. First, an average steepness parameter is calculated as $s_P = H_S/L_P$, where L_P is the length of the linear wave associated with the spectral peak period. If the steepness $s_P \geq 0.04$, the largest force is assumed to come from a large breaking wave, and the slamming load F_B can be computed as

$$F_B = \frac{1}{2}\rho C_S A u^2 \tag{22}$$

$$C_S = 2\pi \tag{23}$$

$$A = \frac{1}{32}H_B D \pi \tag{24}$$

$$u = 1.1 \frac{L_B}{T_B} \tag{25}$$

where

$$T_B = 0.9T_P \quad (26)$$

$$H_B = \min \left[1.4H_S, 0.78h, L_B \cdot \tanh \left(\frac{2\pi h}{L_B} \right) \right] \quad (27)$$

In the above equations, ρ is the density of the fluid, C_S is the slamming coefficient by Goda et al. [27], while D is the cylinder diameter. If $s_P < 0.04$, the load is computed by using the standard Morison equation. The impulsive slamming load is to be applied on top of the quasi-static background load when the wave crest first touches the structure.

5.4. Linear and Second-order irregular waves

Another widely used methodology to simulate nonlinearity in extreme sea states is the second-order irregular wave theory by Sharma and Dean [24], which accounts for a mild nonlinearity in the wave kinematics together with the stochastic nature of the process. Here, 12 different 1-hr realizations of the same sea state are performed and stacked together to obtain a 12-hr total time series. To generate the spectrum, a return period of $T_{\text{ret}} = 3600.0[s]$ was used. The high cut-off of the spectrum was $f_{\text{hc}} = 1/3[Hz]$, consistently with the OceanWave3D simulations, while the time domain signal resolution was $\Delta t = 0.5[s]$.

A total of $n_z = 20$ points was used to compute the wave kinematics, evenly distributed from the sea bottom to the still water line (SWL). We use both the first-order and the first- plus second-order kinematics to compute the horizontal force on the stiff cylinder via the Rainey force model. The kinematics are extrapolated above SWL consistently up to second-order [11]. The first-order kinematics is linearly extrapolated up to the first-order wave elevation, while the second-order kinematics is integrated only up to the SWL.

5.5. Comparison

To compare the results, we have chosen the two significant wave heights associated with tests 11 and 23 from Table 3, corresponding to 100-yr return sea states.

In Figure 13, the modelled free surface elevation signals for experiment 11 are compared. In black, twelve 1-hr long linear realizations were combined to

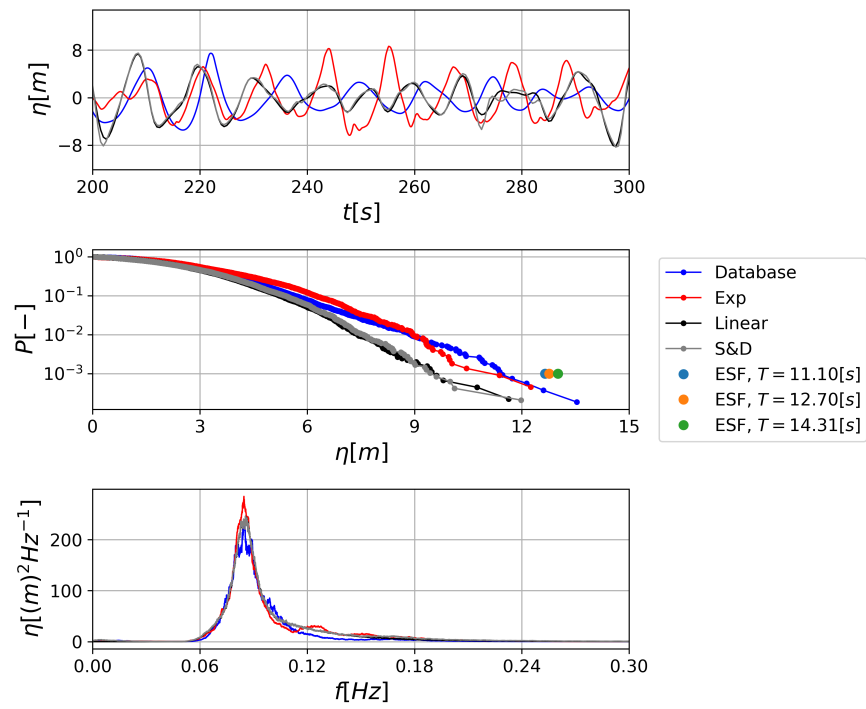


Figure 13: Experiment 11. Comparison of the experimental free surface elevation with the design methodologies.

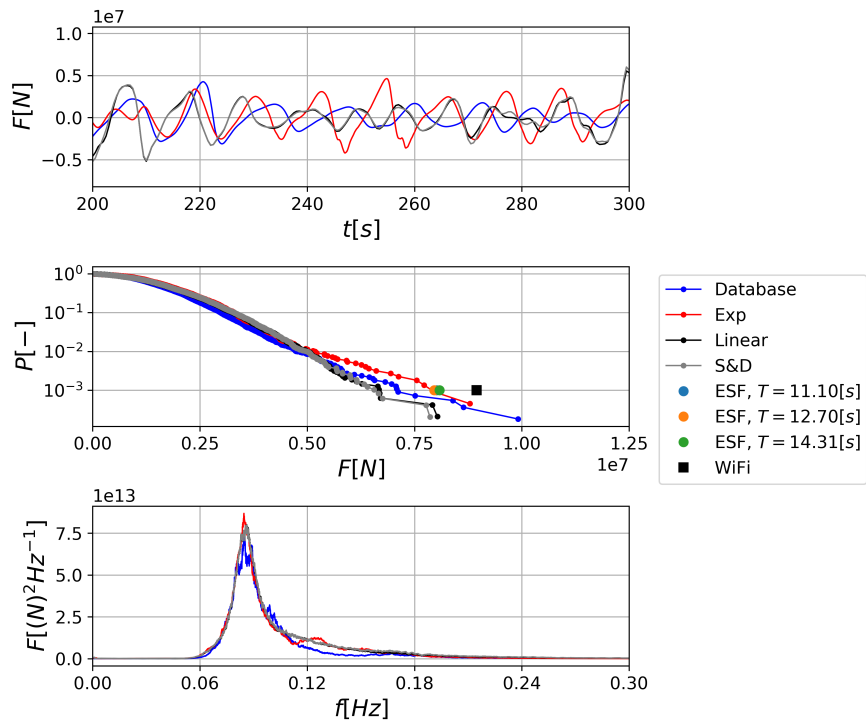


Figure 14: Experiment 11. Comparison of the experimental inline force with the design methodologies.

obtain the linear computation. In gray, the Sharma and Dean second-order contribution was added to the linear one. Five different computations were extracted from the database, which, after disregarding the transients and applying the scaling procedure, yields a time series of roughly 16 hours, in blue.

In Figure 13(b), the main population of the samples in the database crest distribution is in line with the experimental results, down to the extreme crest heights for $P = 1.0 \cdot 10^{-3}$. On the other hand, the largest ESF wave crest is conservative. As for the power spectra, we notice a satisfactory agreement across the frequency span for all of the methods. The Sharma and Dean solution matches the experimental superharmonic energy distribution best, but is the least accurate in predicting the free surface elevation crest distribution.

As for the force crest distribution, in Figure 14, all of the methods perform fairly well down to a probability of 10^{-2} . The ESF method is able to catch the experimental force very well, while the WiFi prediction is slightly conservative. The other methods underestimate the force peak by 20%. This is expected, as by analysis of the force time series it was seen that the experimental event with $P = 1 \cdot 10^{-3}$ was associated with a breaking event inducing a slamming load.

In Figure 15, we observe the results for a 100-yr storm in a shallower depth $h = 20.0[m]$. For a $P = 1 \cdot 10^{-3}$, the predictions from fully-nonlinear methodologies agree much better with the experiments than the linear and the Sharma and Dean solutions. The ESF method predicts a largest crest of about $10.0[m]$ for $P = 1 \cdot 10^{-3}$, which is rather conservative. As for the power spectra, the superharmonic energy distribution is well predicted by the database results, although the energy at the peak frequency is overestimated. The contrary is true for the linear and the Sharma and Dean solution, which capture the peak energy but not the decay rate of energy at the superharmonic frequency. In Figure 16, the peak force distribution computed from the database kinematics agrees well with the experiments around the $P = 1 \cdot 10^{-3}$ level, while the linear and the Sharma and Dean results are nonconservative. Since the average wave steepness was $H_S/L_P = 0.038$, the WiFi model did not predict that the largest load would come from a breaking event.

The crests with a $P = 1 \cdot 10^{-3}$ are summarized in Table 5 for all of the cases. The picture is consistent with our previous analysis: the results from the DeRisk database are the closest to the experimental results, while the

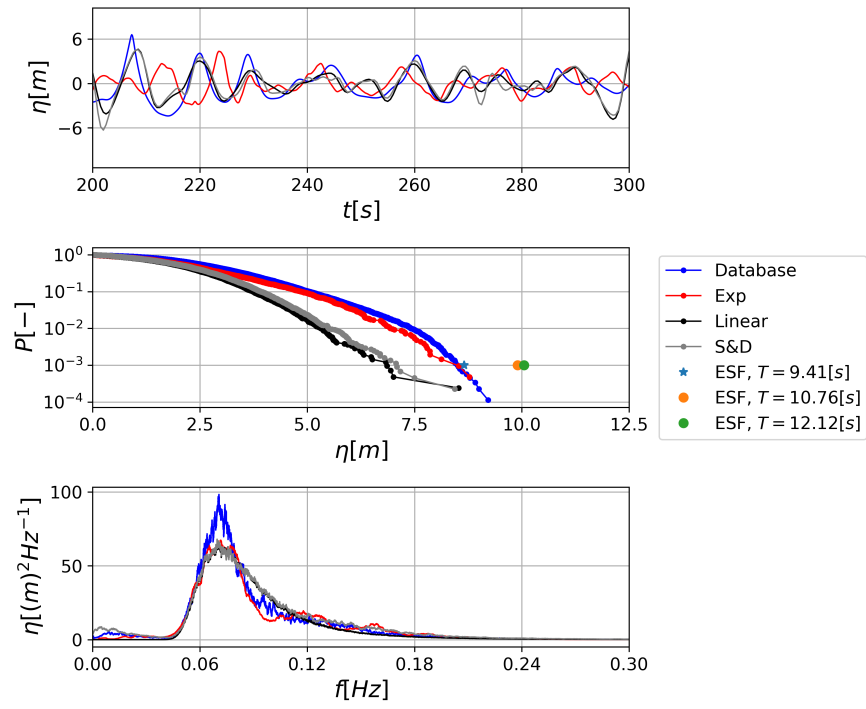


Figure 15: Experiment 23. Comparison of the experimental free surface elevation with the design methodologies.

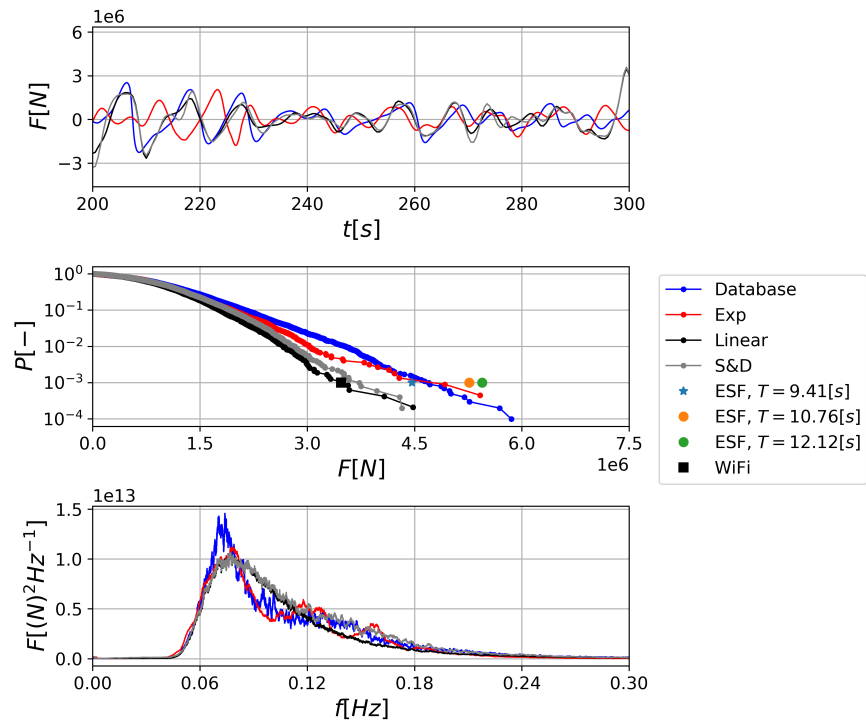


Figure 16: Experiment 23. Comparison of the experimental inline force with the design methodologies.

		Experiments														
No.		1	9	10	10	11	11	12	12	13	20	21	22	23	24	25
Ret [yr]		10	10	10	10	100	100	100	100	1000	10	10	100	100	1000	1000
Depth [m]		33.0	33.0	33.0	33.0	33.0	33.0	33.0	33.0	33.0	20.0	20.0	20.0	20.0	20.0	20.0
$h/gT_P^2 \cdot 10^2$		2.23	2.70	1.82	1.82	2.49	1.82	1.80	1.80	1.39	1.32	1.32	1.36	1.03	1.03	2.62
$H_S/gT_P^2 \cdot 10^3$		6.17	6.37	4.05	4.05	7.41	5.05	5.59	5.59	4.21	4.08	4.08	4.82	3.63	3.95	7.98
Exp		10.54	9.70	8.71	8.71	11.37	10.73	11.59	11.59	6.76	7.33	7.33	7.64	8.53	9.47	6.73
Database		10.86	9.02	9.37	9.37	11.46	10.76	11.54	11.54	6.85	6.85	7.51	8.38	8.50	8.69	6.60
Linear		8.92	7.28	6.77	6.77	9.61	8.94	10.24	10.24	5.62	5.73	5.73	6.53	6.86	7.45	5.49
S&D		8.68	7.37	7.03	7.03	9.44	8.75	9.95	9.95	5.97	6.15	6.15	7.05	7.09	7.69	5.50
ESF		11.73	9.26	8.65	8.65	13.01	11.85	13.86	13.86	7.85	8.29	8.29	10.16	10.05	9.25	8.15

Table 5: Maximum free surface elevation $\eta_{max}[m]$, corresponding to an exceedance probability level of $P = 1 \cdot 10^{-3}$.

embedded stream function predictions are almost consistently conservative. The linear and the Sharma and Dean wave theories always provide too low crest estimates.

In Table 6 we summarize the force peaks with a $P = 1 \cdot 10^{-3}$. For the milder storms with a return time of 10 years, both at the shallow and the deep location, all methods are quite comparable. An exception is made for the WiFi method, which is sensitive to the average sea steepness. For example, in tests 10 and 20 the breaking wave load is not triggered, contrarily to tests 1 and 9, where it leads to an overestimation of the experimental load. For these small storms, the linear and the Sharma and Dean force predictions are acceptable, and not far from the fully nonlinear kinematics ones.

For the 100 years storms, the linear and the Sharma and Dean predictions are too nonconservative. The DeRisk database results agree better for the shallow than for the deep location. This is because in tests 11 and 12, where waves are on average steeper than in tests 22 and 23, slamming loads from breaking waves are more frequent. The ESF method performs better than the WiFi model, which seems to provide conservative estimates, as also observed by de Ridder et al. [23]. As for the 1000 year return storms, none of the models is clearly superior to the others. At $h = 20.0[m]$, all models output similar predictions for case 25, while for case 24 all the methods underpredict the measured forces.

The application of a slamming model in combination with the database is part of our current work. Initial results are published in Pierella et al. [22], and these show that the force predictions from the database can be improved if a breaking wave load is added to the quasi-static load.

6. Conclusion

In this work, we established a database of nonlinear wave kinematics for ultimate load state computations. Different realizations of nonlinear waves are easily extracted from the database, and coupled with a force model to compute loads on slender offshore structures. We demonstrated that the validity of the database is extended by applying the Froude hypothesis to scale the database kinematics to match the required application scale.

Through computations on a flat bed domain, we investigated the effect of the breaking filter on the crest statistics. By comparison with experimental data, we found that a value of $\beta = 0.5$ gave the best agreement. When using the nonlinear kinematics to reproduce the horizontal force from experiments

Experiments														
No.	1	9	10	10	11	12	13	20	21	22	23	24	25	
Ret [yr]	10	10	10	10	100	100	1000	10	10	100	100	1000	1000	
Depth [m]	33.0	33.0	33.0	33.0	33.0	33.0	33.0	20.0	20.0	20.0	20.0	20.0	20.0	
$h/gT_P^2 \cdot 10^2$	2.23	2.70	1.82	2.49	1.82	1.80	1.80	1.39	1.32	1.36	1.03	1.03	2.62	
$H_S/gT_P^2 \cdot 10^3$	6.17	6.37	4.05	7.41	5.05	5.59	5.59	4.21	4.08	4.82	3.63	3.95	7.98	
Exp	5.88	5.66	4.45	7.96	7.52	9.21	9.21	3.41	3.56	4.29	4.92	6.72	3.32	
Database	6.06	5.03	4.60	7.12	6.08	7.17	7.17	3.39	3.96	4.95	4.70	4.94	3.35	
Linear	5.37	4.74	4.23	6.67	5.41	6.90	6.90	3.26	3.19	3.84	3.47	3.97	3.62	
S&D	5.27	4.69	4.23	6.56	5.35	6.72	6.72	3.42	3.32	4.18	3.73	4.28	3.67	
WiFi	9.55	8.06	4.23	8.95	9.57	10.49	10.49	3.26	3.19	5.37	3.47	5.89	3.71	
ESF	6.78	5.23	4.81	8.08	6.92	9.30	9.30	4.22	4.31	5.82	5.45	4.94	4.09	

Table 6: Maximum inline force, measured in $F_{max}[MN]$, corresponding to an exceedance probability level of $P = 1 \cdot 10^{-3}$. When the maximum load for the WiFi model is associated with a breaking wave, the figure is underlined.

on a stiff monopile, a good agreement was observed. Some discrepancies in the super-harmonic part of the horizontal force spectrum were present. These may result from using linear wave generator theory in the experiments.

The static loads from state-of-the-art design methods were compared to the present method. For milder storms, all the analyzed methods output acceptable results and predicted the experiments well. For larger storms, the database results were consistently better than the linear and the Sharma and Dean predictions, while they generally agreed with the embedded stream function predictions. The WiFi JIP force model output accurate but slightly conservative predictions at 33.0[m] depth, while it was generally nonconservative at 20.0[m] depth.

In the next phase of the DeRisk project, the database will be extended to directional seas. Further work will also be done to optimize the procedure outlined in Pierella et al. [22] to compute slamming loads directly from the database results by using the pressure impulse model by Ghadirian and Bredmose [28].

7. Online availability

The DeRisk database is freely available at https://data.dtu.dk/articles/The_DeRisk_Database/10322033. In the event of publication of work resulting from the use of the model, appropriate referencing to the dataset [10] and this paper should be included.

8. Acknowledgements

This work was performed in the framework of the Danish Innovation Fund project DeRisk, grant no. 4106-00038B.

References

- [1] International Electrotechnical Commission, Wind energy generation systems - Part 1: Design requirements, Technical Report, IEC, Geneva, CH, 2019.
- [2] P. J. Rainey, T. R. Camp, Constrained non-linear waves for offshore wind turbine design, in: Journal of Physics, volume 75, IOP Publishing, p. 12067.

- [3] P. S. Tromans, A. R. Anatrak, P. Hagemeyer, New Model for the Kinematics of Large Ocean Waves Application as a Design Wave, in: Proceedings of the First International Offshore and Polar Engineering Conference, volume 8, International Society of Offshore and Polar Engineers, pp. 64–71.
- [4] F. Pierella, R. Stenbro, L. Oggiano, J. D. Vaal, T. A. Nygaard, Stream Function Wave Embedment into Linear Irregular Seas : A New Method Based on the Hilbert Transform, in: Proceedings of the International Offshore and Polar Engineering Conference, pp. 412–419.
- [5] H. Bredmose, J. Mariegaard, B. T. Paulsen, B. Jensen, S. Schløer, T. Larsen, T. Kim, A. M. Hansen, The Wave Loads project, Technical Report, DTU Wind Energy, 2013.
- [6] B. T. Paulsen, H. Bredmose, H. B. Bingham, S. Schløer, Steep Wave Loads From Irregular Waves on an Offshore Wind Turbine Foundation: Computation and Experiment, in: Volume 9: Odd M. Faltinsen Honoring Symposium on Marine Hydrodynamics, American Society of Mechanical Engineers, p. V009T12A028.
- [7] A. P. Engsig-Karup, H. B. Bingham, O. Lindberg, An efficient flexible-order model for 3D nonlinear water waves, *Journal of Computational Physics* 228 (2009) 2100–2118.
- [8] H. Jasak, A. Jemcov, Z. Tukovic, OpenFOAM : A C ++ Library for Complex Physics Simulations, *International Workshop on Coupled Methods in Numerical Dynamics m* (2007) 1–20.
- [9] H. Bredmose, M. Dixen, A. Ghadirian, T. J. Larsen, S. Schløer, S. J. Andersen, S. Wang, H. B. Bingham, O. Lindberg, E. D. Christensen, M. H. Vested, S. Carstensen, A. P. Engsig-Karup, O. S. Petersen, H. F. Hansen, J. S. Mariegaard, P. H. Taylor, T. A. Adcock, C. Obhrai, O. T. Gudmestad, N. J. Tarp-Johansen, C. P. Meyer, J. R. Krokstad, L. Suja-Thauvin, T. D. Hanson, J. Torben, B. Harry, E. Damgaard, A. Peter, O. Skov, J. Sandvig, N. Jacob, DeRisk - Accurate Prediction of ULS Wave Loads. Outlook and First Results, in: *Energy Procedia*, volume 94, Elsevier, 2016, pp. 379–387.

- [10] F. Pierella, O. Lindberg, H. Bredmose, H. B. Bingham, R. Read, A. P. Engsig-Karup, The DeRisk Database dataset, 2020. Available online at https://data.dtu.dk/articles/The_DeRisk_Database/10322033/, DOI:10.11583/DTU.10322033.v1 [dataset].
- [11] Det Norske Veritas, Environmental conditions and environmental loads, Technical Report October, DNV, 2010.
- [12] D. Clamond, D. Fructus, J. Grue, Ø. Kristiansen, An efficient model for three-dimensional surface wave simulations. Part II: Generation and absorption, *Journal of Computational Physics* (2005).
- [13] S. Schløer, H. Bredmose, A. Ghadirian, Experimental and Numerical Statistics of Storm Wave Forces on a Monopile in Uni- and Multidirectional Seas, in: *Ocean Renewable Energy*, volume 10, ASME, 2017, p. V010T09A073.
- [14] A. Ghadirian, H. Bredmose, Investigation of the effect of the bed slope on extreme waves using First Order Reliability Method, *Marine Structures* 67 (2019) 102627.
- [15] S. Schløer, Fatigue and extreme wave loads on bottom fixed offshore wind turbines. Effects from fully nonlinear wave forcing on the structural dynamics, Ph.D. thesis, DTU, 2013.
- [16] R. C. T. Rainey, Slender-Body Expressions for the Wave Load on Offshore Structures, *Proceedings of the Royal Society A: Mathematical, Physical and Engineering Sciences* 450 (1995) 391–416.
- [17] T. Kristiansen, O. M. Faltinsen, Higher harmonic wave loads on a vertical cylinder in finite water depth, *Journal of Fluid Mechanics* 833 (2017) 773–805.
- [18] L. Suja-Thauvin, E. Bachynski, F. Pierella, M. Borg, J. Krokstad, H. Bredmose, Critical assessment of hydrodynamic load models for a monopile structure in finite water depth, 2020. Submitted for publication.
- [19] P. W. Bearman, M. J. Downie, J. M. R. Graham, E. D. Obajasu, Force on a circular cylinder in viscous oscillatory flow at low keulegan—carpenter numbers, *Journal of Fluid Mechanics* 165 (1986) 61–71.

- [20] R. Longoria, J. Beaman, R. Miksad, An experimental investigation of forces induced on cylinders by random oscillatory flow, *Journal of Offshore Mechanics and Arctic Engineering* 115 (1993) 23–30.
- [21] B. M. Sumer, J. Fredsøe, *Hydrodynamics around cylindrical structures*, World Scientific Pub, 2006.
- [22] F. Pierella, A. Ghadirian, H. Bredmose, Extreme Wave Loads on Monopile Substructures: Precomputed Kinematics Coupled With the Pressure Impulse Slamming Load Model, 2019. V001T01A011.
- [23] E. J. de Ridder, T. Bunnik, J. M. Peeringa, B. T. Paulsen, C. Wehmeyer, P. Gujer, E. Asp, Summary of the Joint Industry Project Wave Impact on Fixed Foundations (WiFi JIP), ASME International, 2017, p. V010T09A081.
- [24] J. N. Sharma, R. G. Dean, Second-Order Directional Seas and Associated Wave Forces, *Society of Petroleum Engineers Journal* 21 (1981) 129–140.
- [25] R. C. Rainey, Weak or strong nonlinearity: The vital issue, *Journal of Engineering Mathematics* 58 (2007) 229–249.
- [26] S. Wang, T. J. Larsen, H. Bredmose, Ultimate load analysis of a 10 MW offshore monopile wind turbine incorporating fully nonlinear irregular waves, 2020. Submitted for publication.
- [27] Y. Goda, S. Haranaka, M. Kitahata, Study on impulsive breaking wave forces on piles, *Report Port and Harbour Technical Research Institute* 6 (1966) 1–30.
- [28] A. Ghadirian, H. Bredmose, Pressure impulse theory for a slamming wave on a vertical circular cylinder, *Journal of Fluid Mechanics* 867 (2019) R1–1 – R1–14.